AERO 523 Project 3 – Flow over a Three-Element Airfoil

Enoch Lee

Introduction

In project 3, the first and second-order finite volume method were used to solve for compressible, subsonic flow over a three-element, high-lift airfoil. Four different meshes, with an element count of 1149, 2116, 4124, and 8031 respectively, were used in the simulation to generate contour plots of pressure distribution, Mach number, and streamline distribution. The forces, namely lift and drag, were also computed in the post-processing calculations.
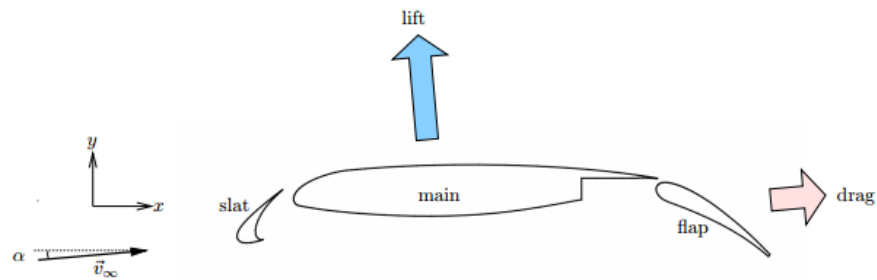

Figure 1: Geometry and output definitions for a three-element airfoil.

The geometry of the airfoil, which consists of three elements, namely slat, main, and flap, is given in Fig. (1) and the four computational domains are given in Fig. (2). The definitions of the meshes were provided by the project statement.
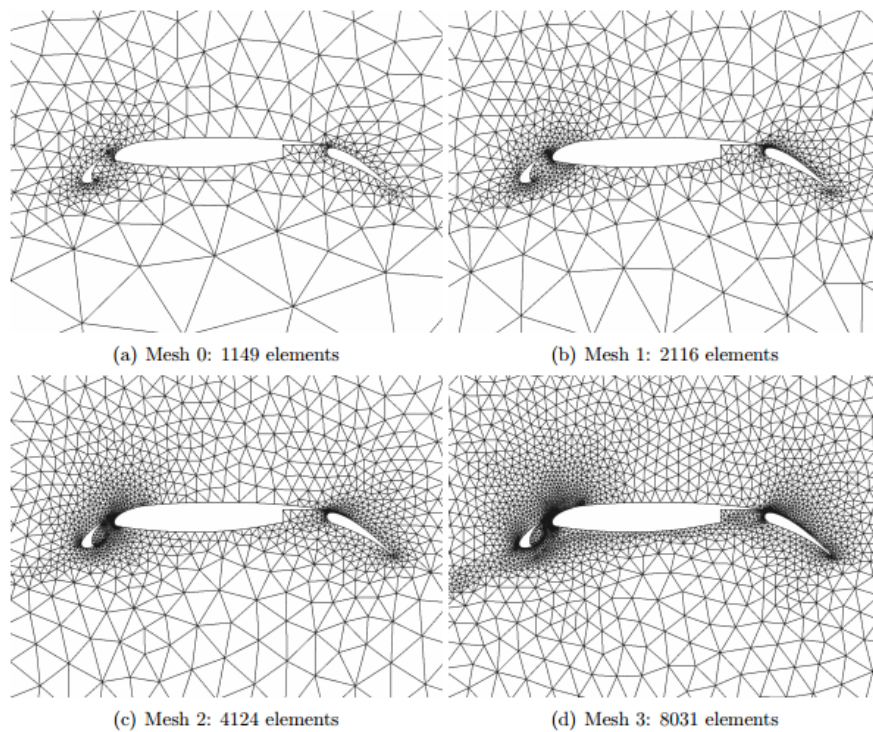

Figure 2: The magnified view of the four provided computational meshes.

Methodology

In order to solve for forces and pressure distribution, the conservative and compressible Euler equations of gas dynamics that govern the flow of a perfectly inviscid gas were used as the core equations in the simulation. This is given by the following expression

$$\frac{\partial u}{\partial t} + \nabla \cdot \vec{F} = 0 \tag{1}$$

where u is the conservative state vector and $\vec{F}$ is the flux that describes the direction and rate at which the conserved quantities are passing through the computational cell.

The conservative state vector is given by

$$u = [\rho, \rho u, \rho v, \rho E]^T = \left[1, M \cos \alpha, M \sin \alpha, \frac{1}{\gamma(\gamma-1)} + \frac{M^2}{2} \right]^T \tag{2}$$

where M is the Mach number, γ is the specific heat ratio of air defined to be 1.4, and α is the angle of attack defined to be 5°. The state vector in Eq. (2) contains quantities of mass, x-momentum, y-momentum, and energy respectively. For the purpose of this simulation, the freestream Mach number was defined to be 0.25. The state of every cell in the computational domain was then calculated using finite-volume methods and information was extracted and plotted in the subsequent post-processing calculation.

First-Order Finite Volume

Forward Euler was used for the first-order finite volume method. The scheme is given by

$$u_i^{n+1} = u_i^n - \frac{\Delta t_i^n}{A_i} R_i(U^n) \tag{3}$$

where i denotes the cell number, n denotes the iteration step, u_i^{n+1} is the state at cell i at $n+1$ iteration, Δt_i^n is the local time step, A_i is the cell area, and $R_i(U^n)$ is the flux residual at cell i computed from state U^n. The flux residual R_i is defined as follows

$$R_i = \sum_{e=1}^{m} \hat{F}\left(u_i, u_{N(i,e)}, \vec{n}_{i,e}\right) \Delta l_{i,e} \tag{4}$$

where e is the edge index that defines a cell, $N(i,e)$ is the element adjacent to cell i across edge e, $\vec{n}_{i,e}$ is the outward-pointing normal vector from cell i on edge e, and $\Delta l_{i,e}$ is the edge length of edge e in cell i. m denotes the number of edges each cell has. For this project, since triangular cells were used in the mesh, m is defined to be 3. The flux function used in this simulation was given by Roe Flux and the code was provided by the project specifications.

The local time step Δt_i^n in Eq. (3) is defined by

$$\Delta t_i^n = \frac{2 A_i\, CFL}{\sum_{e=1}^{m} |s|_{i,e} \Delta l_{i,e}} \tag{5}$$

where s is the maximum wave speed computed during the flux calculation on each edge. A CFL number of 0.9 was used for all simulations to ensure stability and convergence.

Second-Order Finite Volume

For the second-order method, the total variation diminishing second-order Runge-Kutta scheme was used. The scheme is given by

$$u_i^{FE} = u_i^n - \frac{\Delta t_i^n}{A_i} R_i(U^n) \tag{6}$$

$$u_i^{n+1} = \frac{1}{2}\left[u_i^n + u_i^{FE} - \frac{\Delta t_i^n}{A_i} R_i(U^{FE})\right] \tag{7}$$

where FE refers to Forward Euler method used in the first stage. The same local time step was used in both stages. Note that this time step varies with different cells and their fluxes. In this project, the converged solution from the first-order Forward Euler method was used as the input for the second-order method.

In the second-order finite volume method, a linear representation of the state values inside each cell was used. This was done by computing the average gradient in each cell i, $\nabla u|_i$, by the following expression

$$\nabla u|_i = \frac{1}{A_i} \int_{\partial A} \hat{u}_i \vec{n} ds \tag{8}$$

where $\hat{u}$ is the average state vector of the cell i. This quantity was calculated by taking the arithmetic average of the left/right face neighbors. The gradient was then used to evaluate the cell state vector at each of the edge midpoints by the following relation

$$u(\vec{x}) = u_i + \nabla u|_i \cdot (\vec{x} - \vec{x}_i) \tag{9}$$

where $\vec{x}_i$ is the cell centroid and $\vec{x}$ is the edge midpoint. The resulting left and right states of any particular edge were then inputted to the flux function to get the residual via Eq. (4) and the new state for each cell was then updated.

The convergence for both methods was assessed by monitoring the L_∞ norm of the residual vector, $|R|_{L_\infty}$. While the specification deems a solution converged when $|R|_{L_\infty} < 10^{-7}$, since the residual oscillates because of the propagation of information in the flow field, the convergence criteria for this simulation was wet to be $|R|_{L_\infty} < 10^{-8}$ to ensure all errors will not go above 10^{-7}.

Boundary Conditions

There existed two kinds of boundary conditions in this project. The boundary at the far field and the boundary at the wall of the airfoil. These were treated differently for flux calculations. At the boundary at the farfield, the given Roe Flux function was used. However, different from the interior edges, the freestream state vector was used as the inflow cell. On the other hand, a new wallflux function was written to provide the accurate flux for cells adjacent to the airfoil inviscid walls. The new boundary flux, where the no flow through condition is satisfied, on the wall is given by

$$\hat{F}^b = \left[0, p^b n_x, p^b n_y, 0\right]^T \tag{10}$$

where p^b is the boundary pressure given in Eq. (11) and n is the outward pointing vector that describes the direction of the flux.

Post processing – Pressure, Forces, and Mach numbers

The pressure values were extracted from the converged state vector and forces were computed. The pressure was extracted from the converged solution by the following expression

$$p^b = (\gamma - 1)(\rho E^+ - \frac{1}{2}\rho^+|\vec{v}^b|^2) \tag{11}$$

where the exponent $+$ denotes the average state inside the computational domain and the exponent b denotes the boundary state. This pressure value is calculated inside the wallflux function. The forces of each airfoil component were calculated using the following expression

$$\vec{F}' = \int p\vec{n}dl \tag{12}$$

The total force on the entire airfoil is simply the sum of all forces acting on the components. Eq. (12) decomposes the pressure into x and y components using the normal. Because of a non-zero angle of attack, a coordinate transform has to be performed to extract the lift and drag values. This operation is given by

$$L' = F_y \cos\alpha - F_x \sin\alpha \tag{13}$$

$$D' = F_y \sin\alpha + F_x \cos\alpha \tag{14}$$

These forces, namely lift and drag, as well as the pressure, were non-dimensionalized by the following expressions for presentation purposes

$$c_l = \frac{L'}{\frac{1}{2}\rho_\infty|\vec{v}_\infty|^2 c}, \; c_d = \frac{D'}{\frac{1}{2}\rho_\infty|\vec{v}_\infty|^2 c}, \; c_p = \frac{p-p_\infty}{\frac{1}{2}\rho_\infty|\vec{v}_\infty|^2} \tag{15}$$

where ∞ denotes freestream conditions, ρ is the density, c is the reference chord length which is defined as 0.5588, and $\vec{v}_\infty$ is the freestream velocity.

The Mach number can be computed by the following expression

$$M = \frac{v}{c} \tag{16}$$

where v is the flow velocity and c is the speed of sound. The flow velocity v can be extracted directly from the converged state vector and speed of sound c can be computed by the following relationship

$$c = \sqrt{\frac{\gamma p}{\rho}} \tag{17}$$

The calculation of pressure distribution of the entire flow field is the same as that given in Eq. (11).

Streamlines and Mass flow rate

After the solution has converged, the streamline profiles were computed for all the simulations. By definition, the difference between two streamline is the mass flow rate between the lines. As such, streamline can be calculated by the following relation

$$\psi_2 = \psi_1 + \int_1^2 \rho\vec{v} \cdot \vec{n}dl = \psi_1 + \Delta l \hat{F}_\rho \tag{18}$$

where $\hat{F}_\rho$ is the mass-conservation component of the numerical flux and Δl is the edge length. Since one knows the streamline on the body of the airfoil, which is naught, all the streamlines in the flow field can be specified with the given flux function as well as the converged solution. The graphical representation of this operation is provided in Fig. (3). Like in the calculations of numerical fluxes and residual in the second-order simulations, the streamlines were computed using second-order fluxes, which was done by Eq. (9) and substituting the updated states into the Roe Flux function. This was done to preserve the second-order accuracy of the method in streamlines.
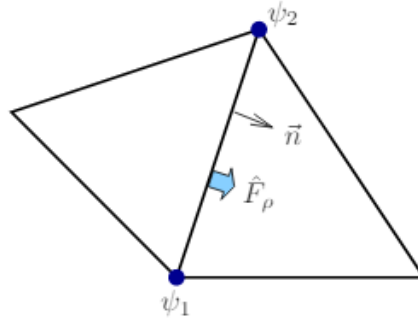
Figure 3: Definitions in the incremental calculation of the stream function ψ.

By the same token, the mass flow rate between any two bodies can be calculated by numerically subtracting two different streamlines. Because streamlines on any surface carry the same value, the stream function on the boundary of another body represents the mass flow rate of air between that body and the reference body, which was set to be the main airfoil and carried the value of 0.

Results & Discussion

The results are presented by mesh cases and order of method used. The four meshes, used in both first-order and second-order simulations, are plotted in Fig. (4), Fig. (11), Fig. (18), and Fig. (25). First half of this section, namely Fig. (4) through Fig. (31), are the results of first-order simulation of the four meshes. The latter half of the section, namely Fig. (32) through Fig. (55) are the results of second-order simulations of the same four meshes. The summary of forces, mass flow rates, and convergence times can be found in Table 1 through Table 4.

The residual convergences are plotted for all eight cases. As one would expect, a larger mesh required more iterations to converge to the same convergence criterion. The residual convergences of all cases show oscillatory behavior, reflecting the way information is propagated in the computational domain during respective simulations. All were able to converge to the convergence criteria without problems.

The lift coefficients for all eight cases are also plotted. In the first-order simulations, lift coefficient convergence started from a lower value and oscillated erratically before converging to a higher value and remained relatively constant midway through the simulations. On the other hand, lift coefficient convergence in the second-order simulations does not oscillate as much as their first-order counterparts, possibly due to the fact that the converged solution is used as the input for the second-order simulations.

The contour plots of Mach numbers for all cases are presented differently, depending if the method used was first or second-order. In the first-order simulations, the converged average cell value was plotted on the triangular mesh. In the second-order simulations, however, the converged states were interpolated between cells using the interp command in MATLAB pdeplot. This is because the calculations were based on a linear representational of state inside each cell, as mentioned in the methodology section. All Mach contour plots showed promising results, with higher Mach numbers at the leading edge of each component and lower values below the components. Increasing mesh sizes correspond to an increase in Mach number in the same region of the computational domain.

Contour plots of pressure distribution for all cases are presented in a similar fashion as that of Mach numbers. All plots showed reasonable results, with a high pressure region below the airfoil and low pressure region on top. As mesh size is increased, the pressure at the same region is also increased.

A detailed view of pressure distribution can be found in the surface pressure distribution plots. The results shown are consistent with what one would expect from a high-lift airfoil. Pressure peaks negatively at the leading edges of the airfoil component then increases along the chord of respective components. The small but noticeable discontinuity in the surface distribution plots is attributable to the separation between airfoil components.

Finally, the streamlines for all cases are plotted using the converged solution. 50 levels of stream functions ranging from -0.1 and 0.1 were plotted. All plots show trends that are consistent. At higher resolutions, that is, larger mesh sizes, streamlines between airfoil components are represented clearer. There existed circulation regions behind the abrupt geometrical indent of the main airfoil as well as behind the slat.
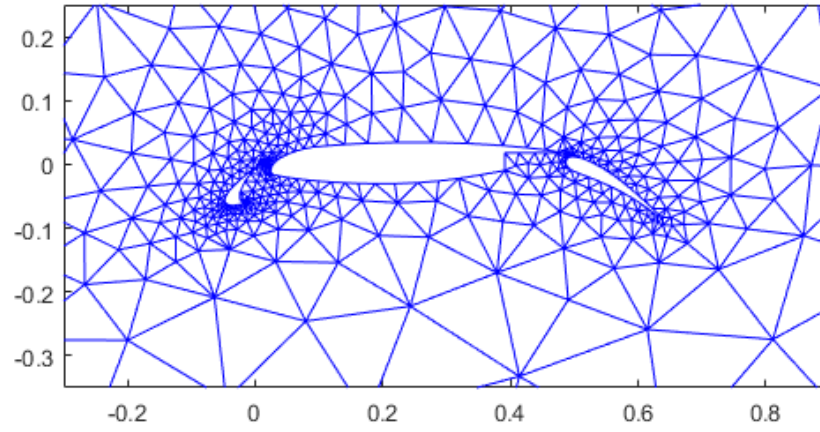
Figure 4: Computational domain, mesh 0, with 1149 elements.
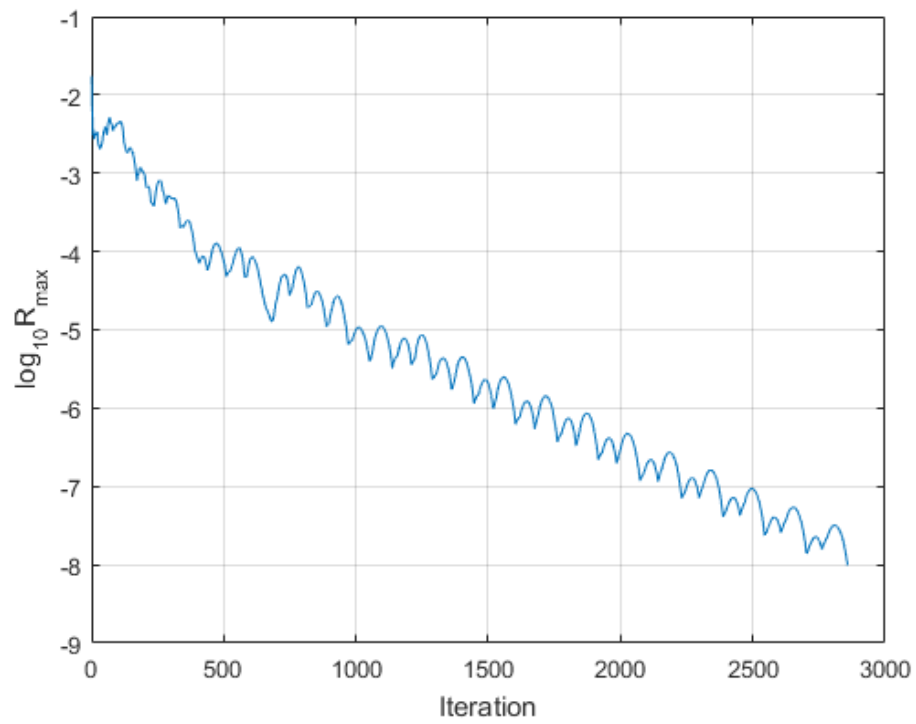
Figure 5: Residual convergence (First-order finite volume, mesh 0)
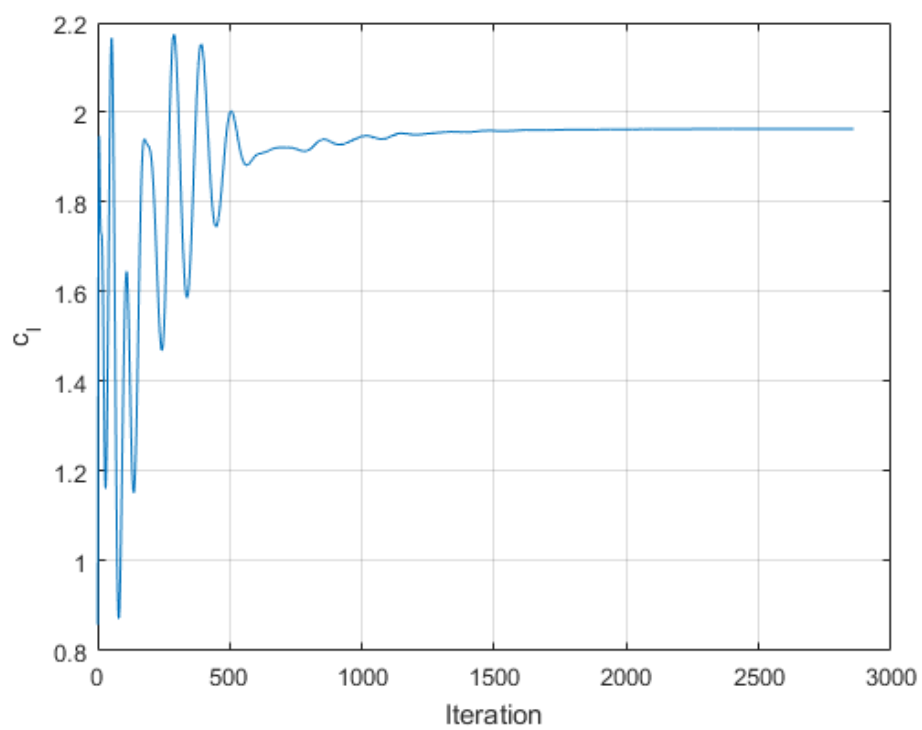
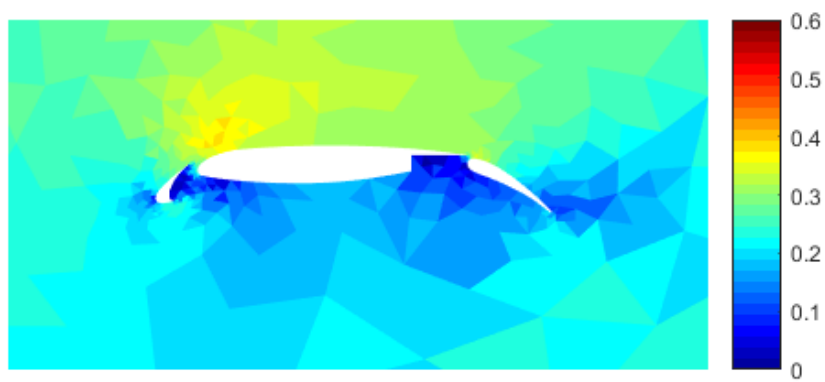Figure 6: Lift coefficient convergence (First-order finite volume, mesh 0)

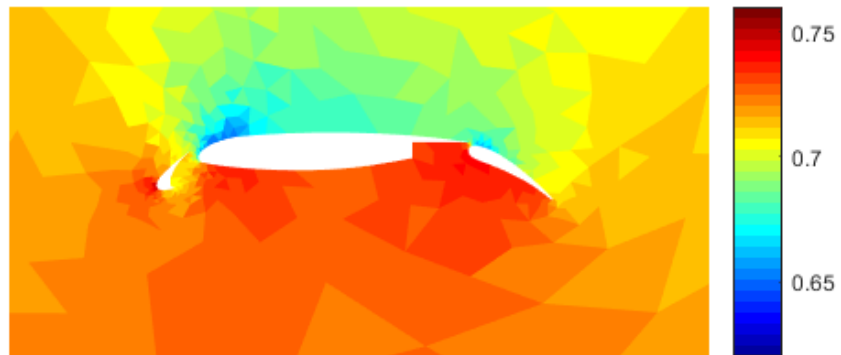Figure 7: Mach number contours (First-order finite volume, mesh 0)

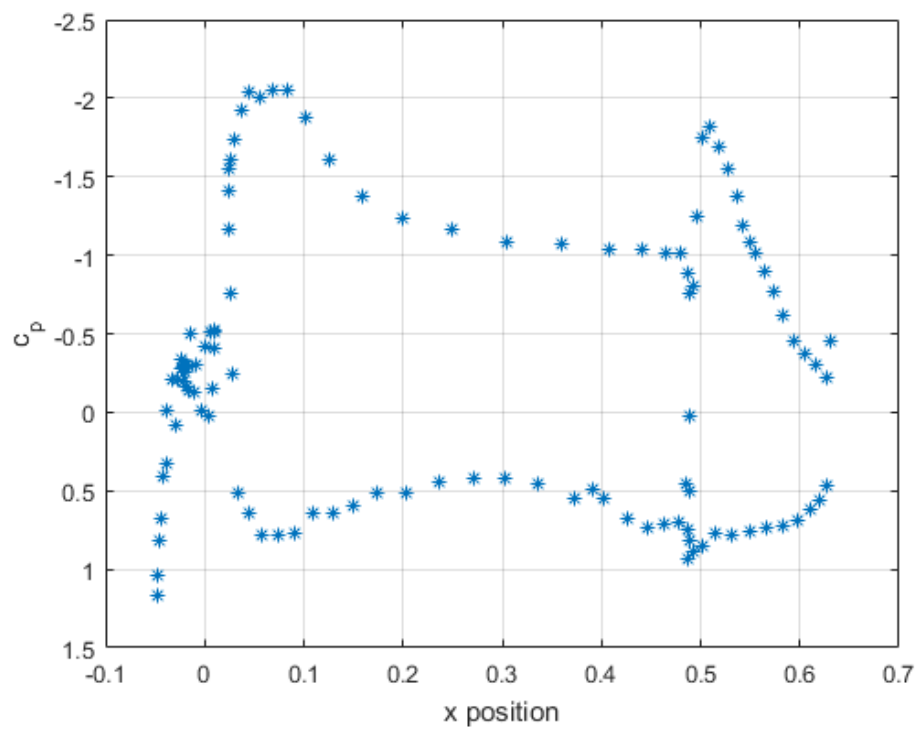Figure 8: Pressure contours (First-order finite volume, mesh 0)

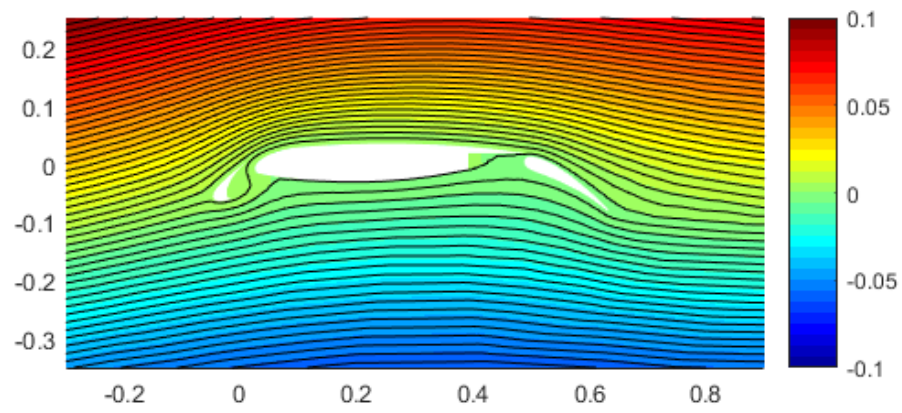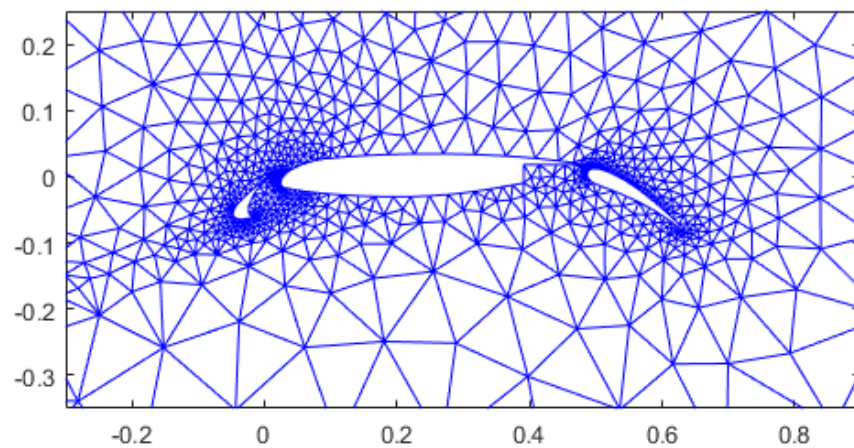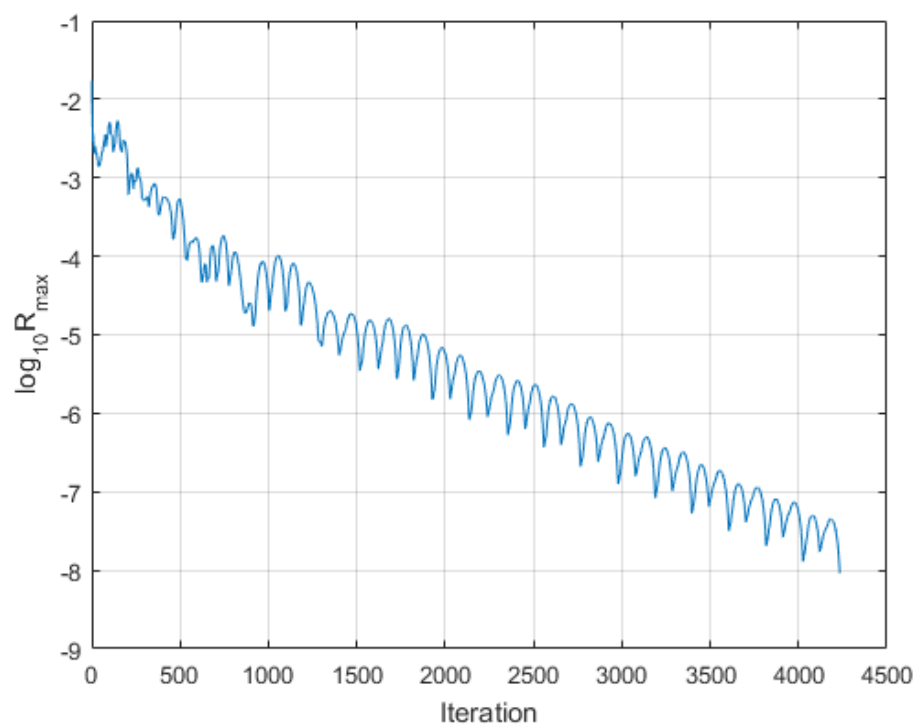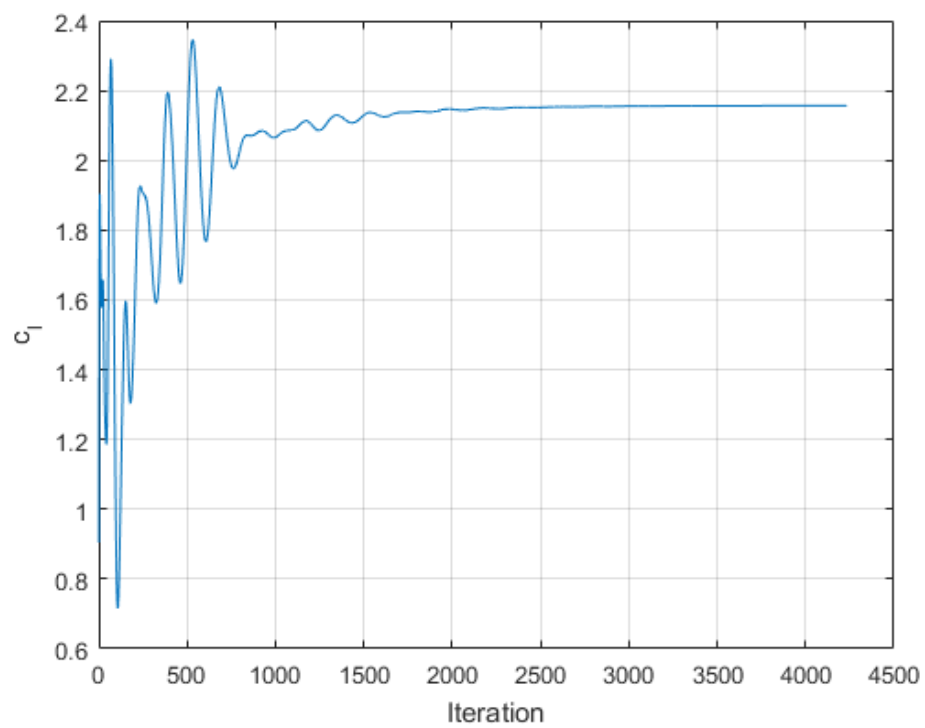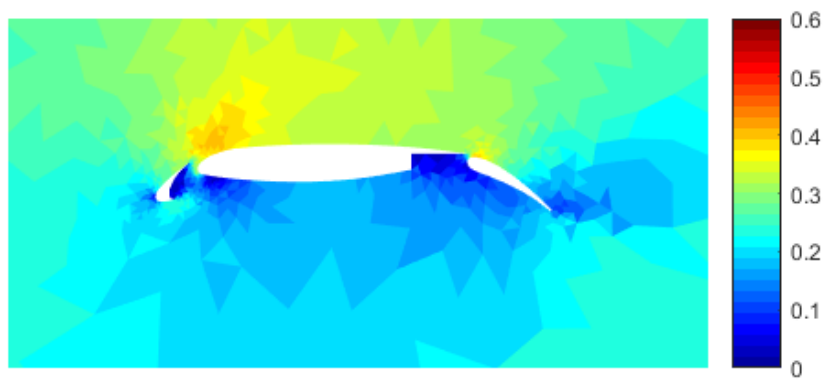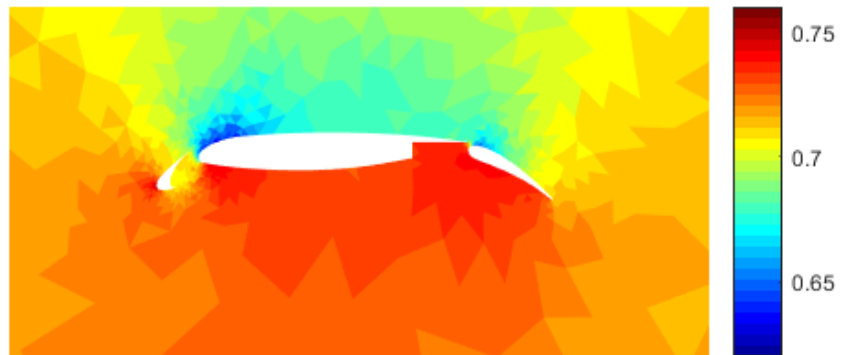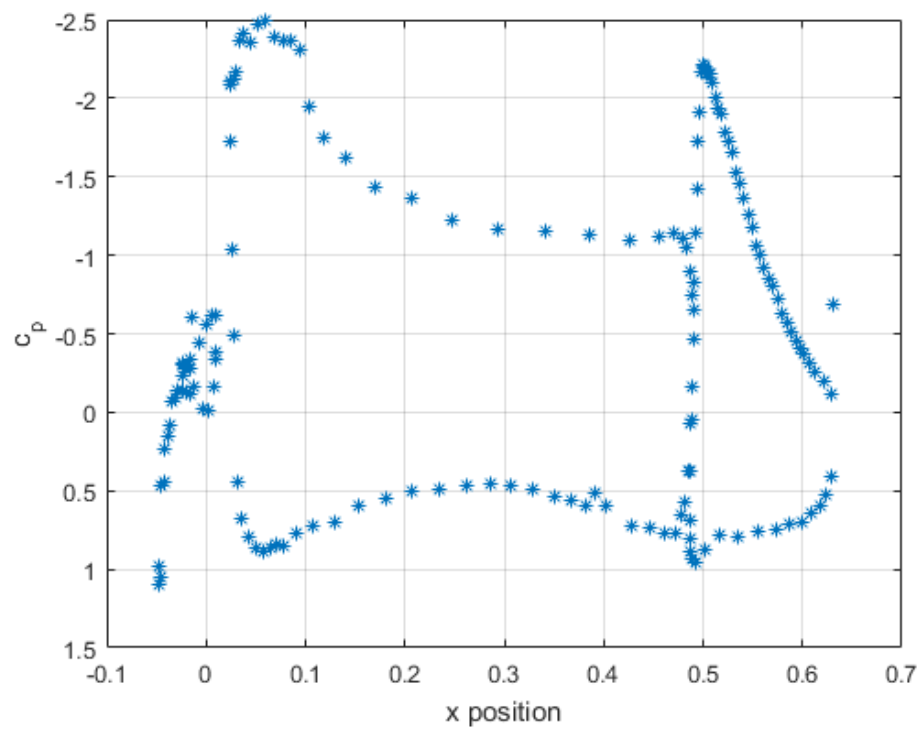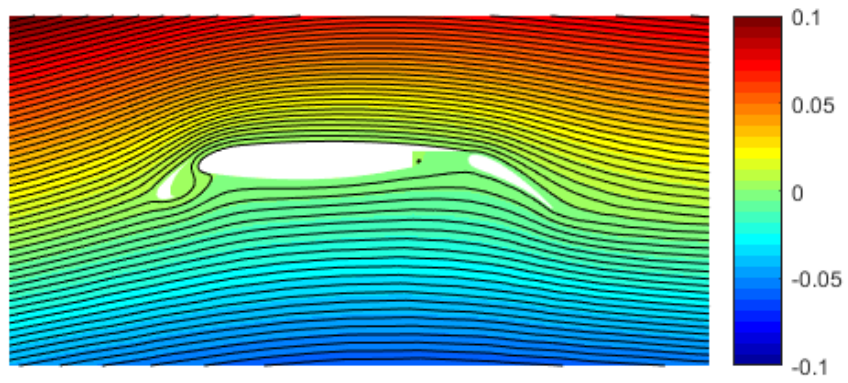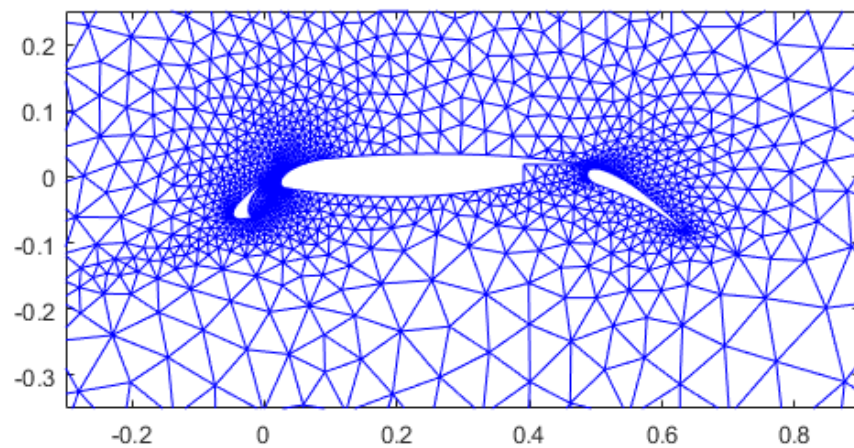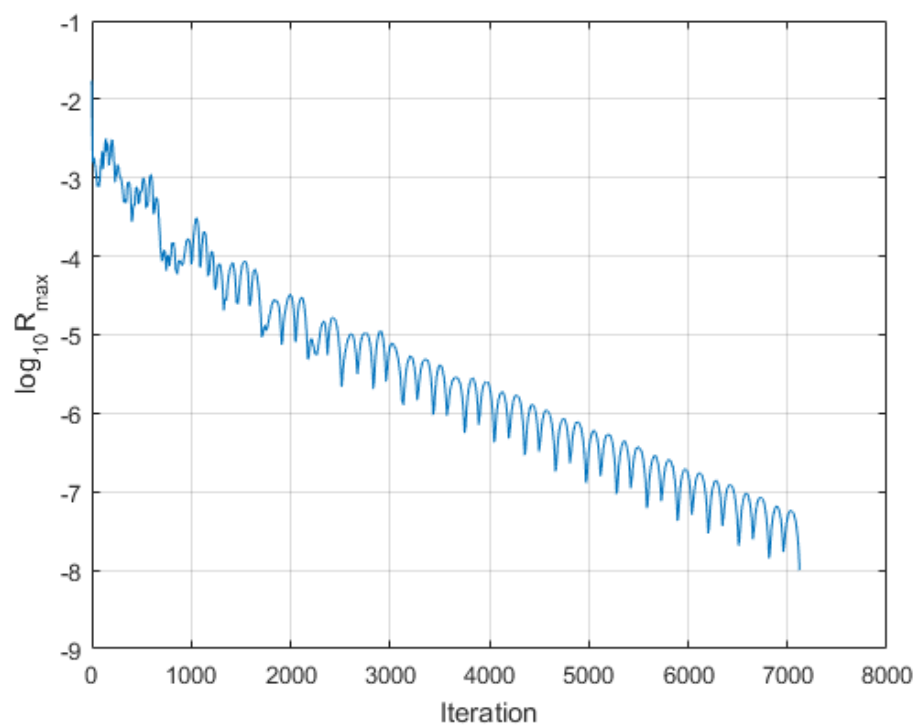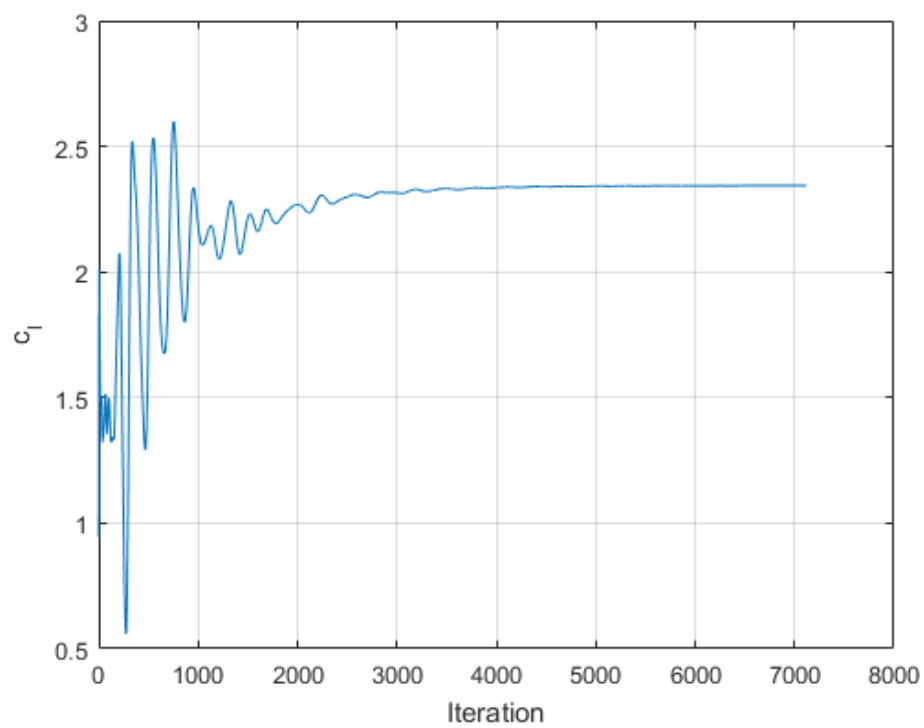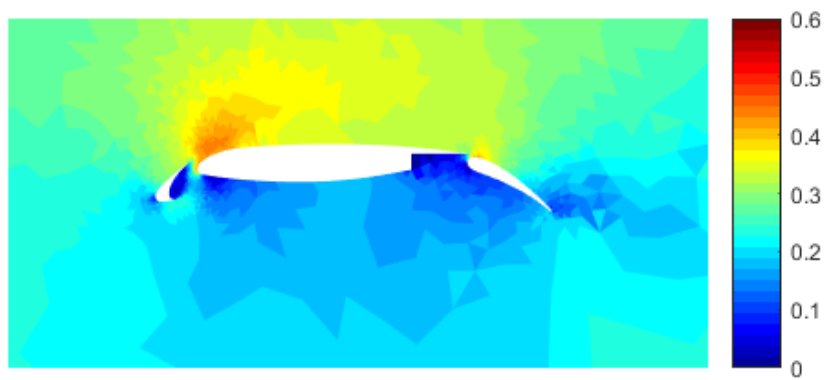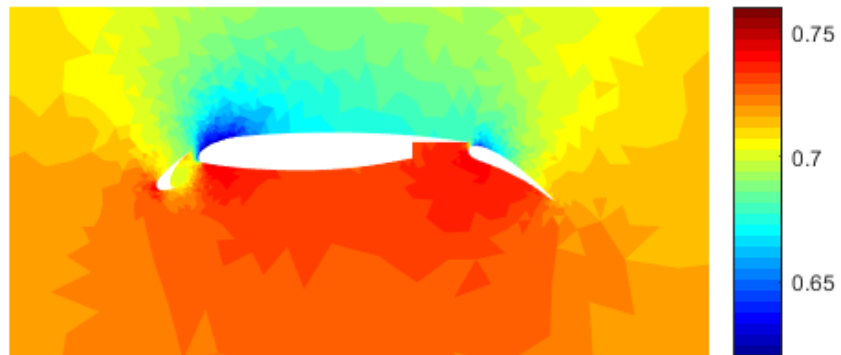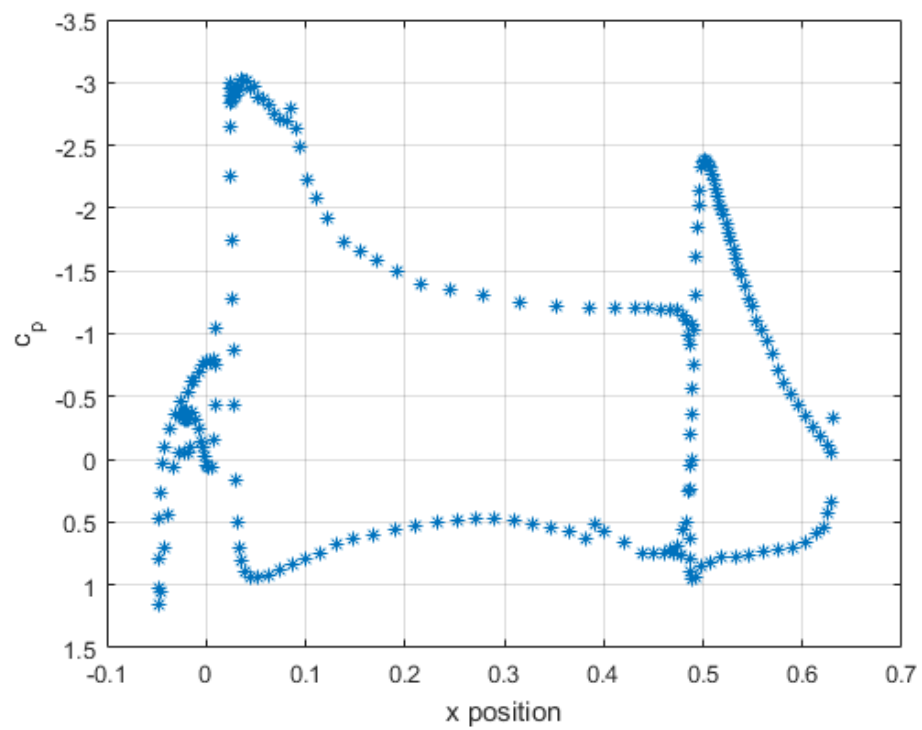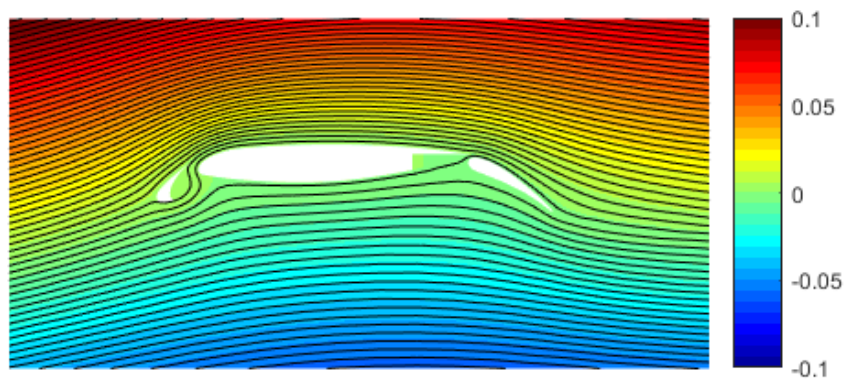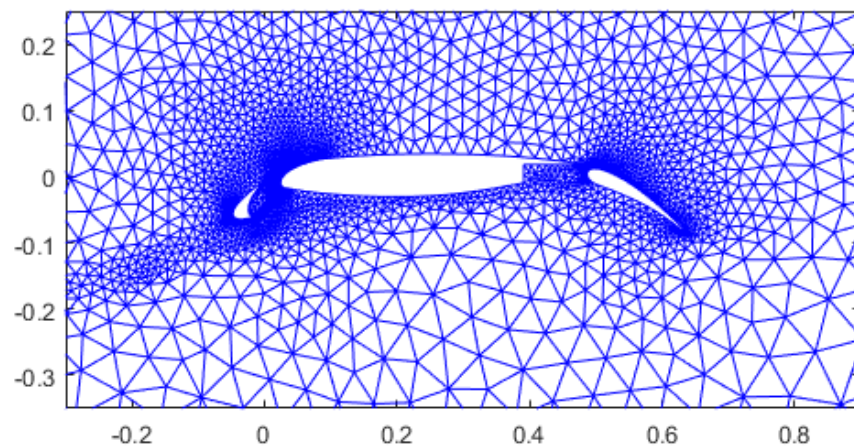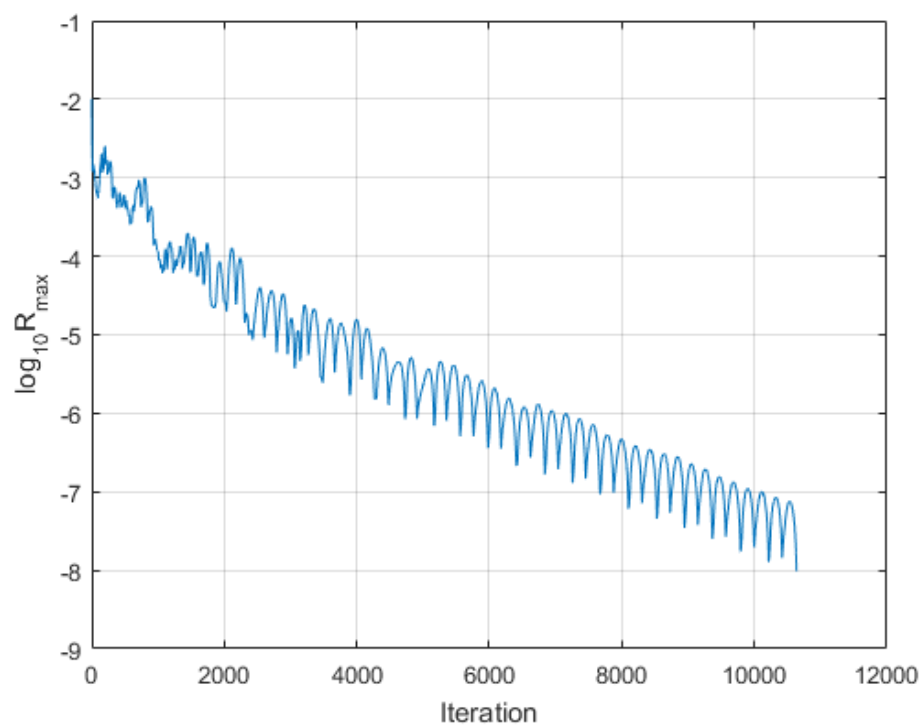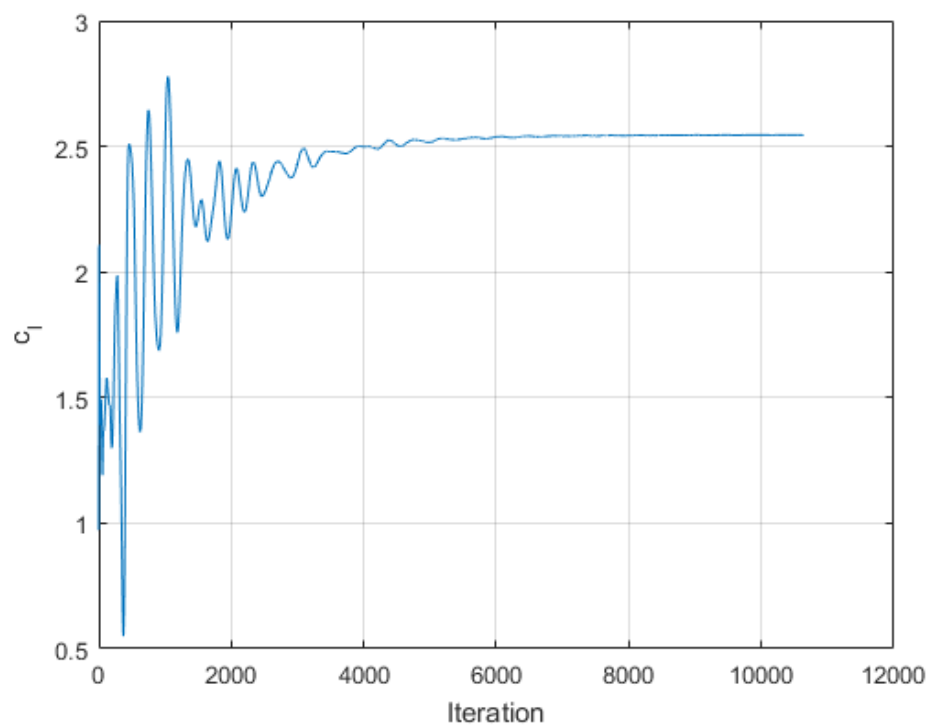Figure 9: Surface pressure coefficient distribution (First-order finite volume, mesh 0)

Figure 10: Streamline (First-order finite volume, mesh 0, 50 contours)

Figure 11: Computational domain, mesh 1, with 2116 elements.

Figure 12: Residual convergence (First-order finite volume, mesh 1)

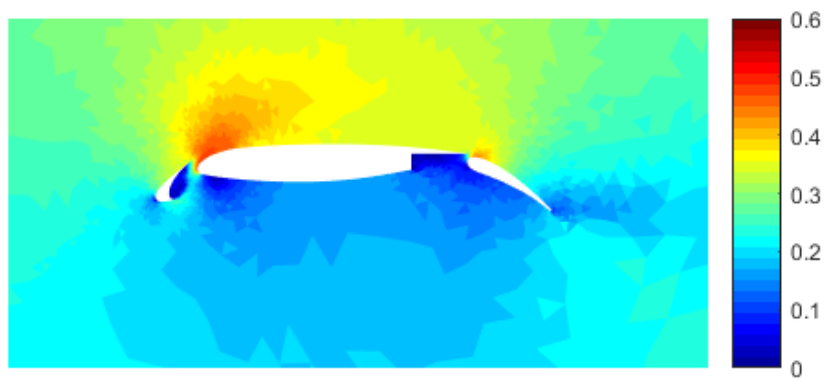Figure 13: Lift coefficient convergence (First-order finite volume, mesh 1)

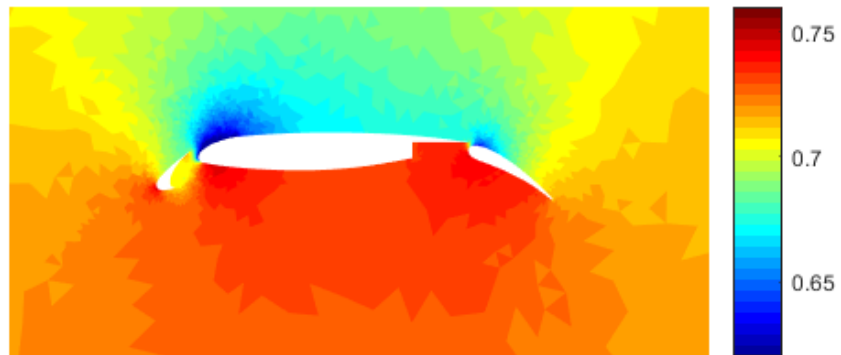Figure 14: Mach number contours (First-order finite volume, mesh 1)

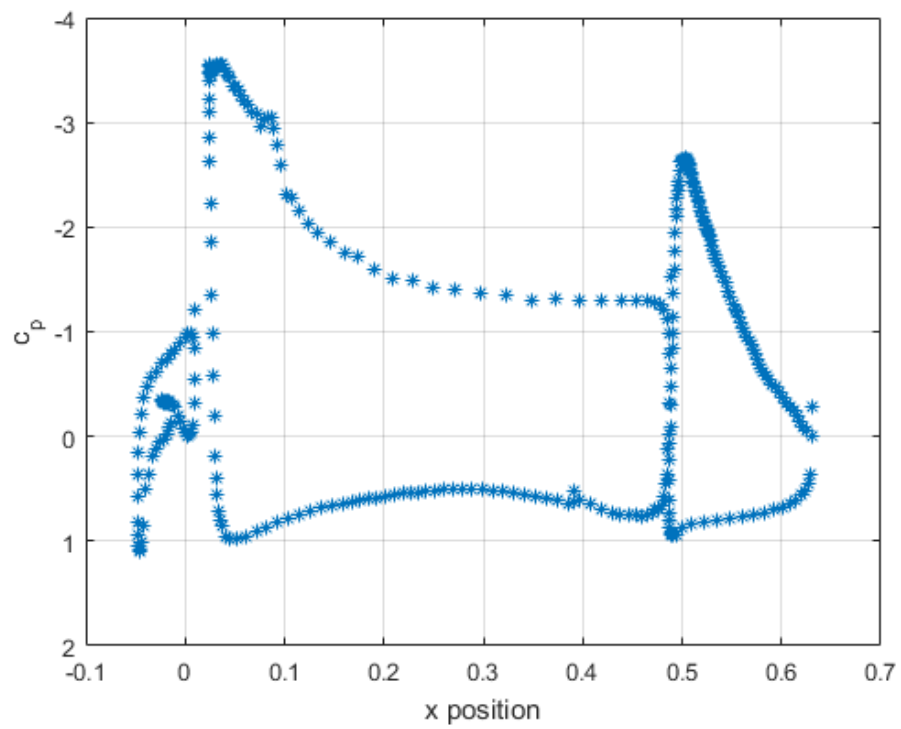Figure 15: Pressure contours (First-order finite volume, mesh 1)

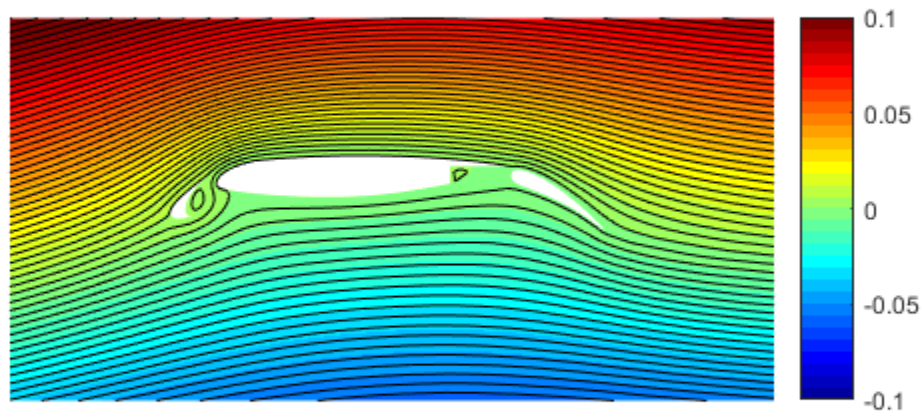Figure 16: Surface pressure coefficient distribution (First-order finite volume, mesh 1)

Figure 17: Streamline (First-order finite volume, mesh 1, 50 contours)

Figure 18: Computational domain, mesh 2, with 4124 elements.

Figure 19: Residual convergence (First-order finite volume, mesh 2)

Figure 20: Lift coefficient convergence (First-order finite volume, mesh 2)

Figure 21: Mach number contours (First-order finite volume, mesh 2)

Figure 22: Pressure contours (First-order finite volume, mesh 2)

Figure 23: Surface pressure coefficient distribution (First-order finite volume, mesh 2)

Figure 24: Streamline (First-order finite volume, mesh 2, 50 contours)

Figure 25: Computational domain, mesh 3, with 8031 elements.

Figure 26: Residual convergence (First-order finite volume, mesh 3)

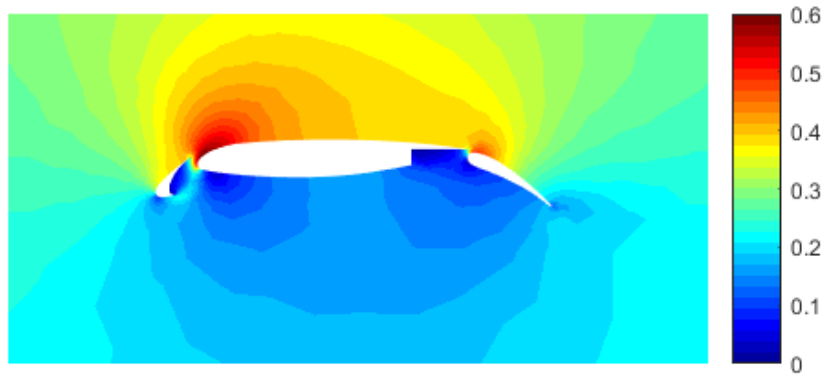Figure 27: Lift coefficient convergence (First-order finite volume, mesh 3)

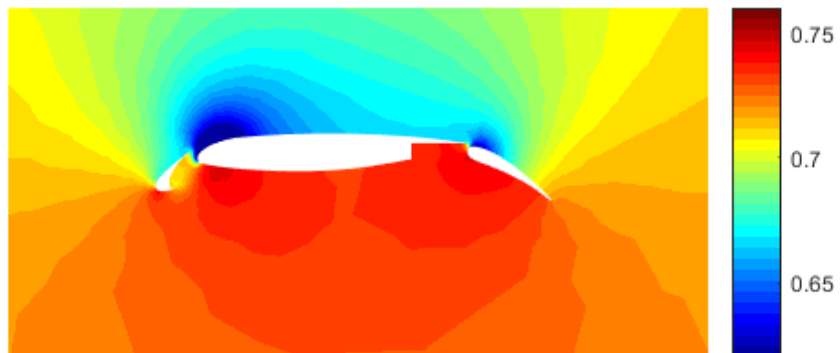Figure 28: Mach number contours (First-order finite volume, mesh 3)

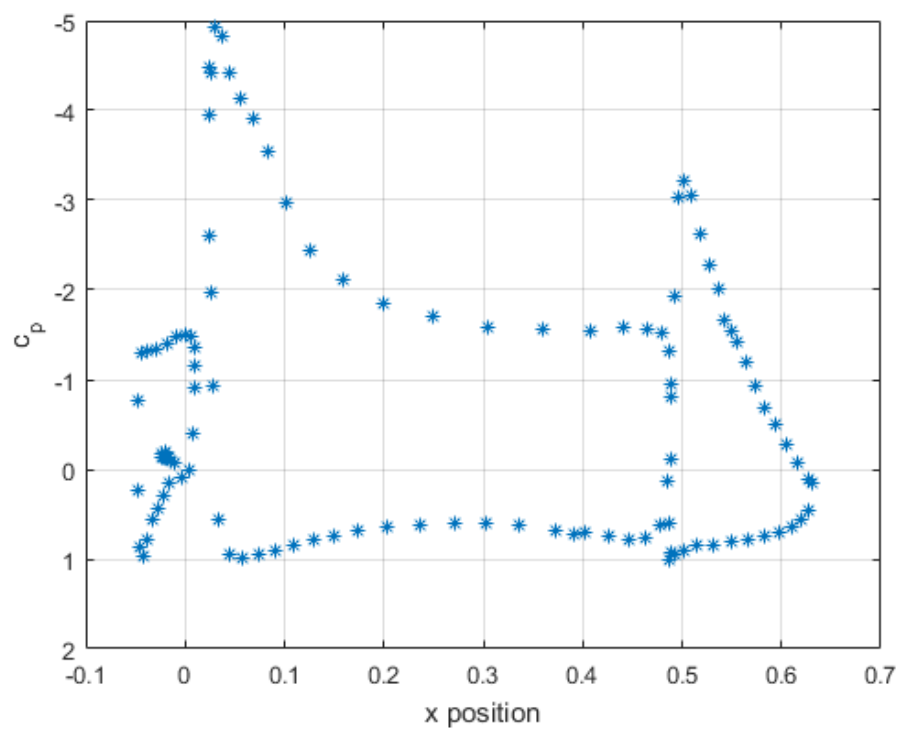Figure 29: Pressure contours (First-order finite volume, mesh 3)

Figure 30: Surface pressure coefficient distribution (First-order finite volume, mesh 3)

Figure 31: Streamline (First-order finite volume, mesh 3, 50 contours)
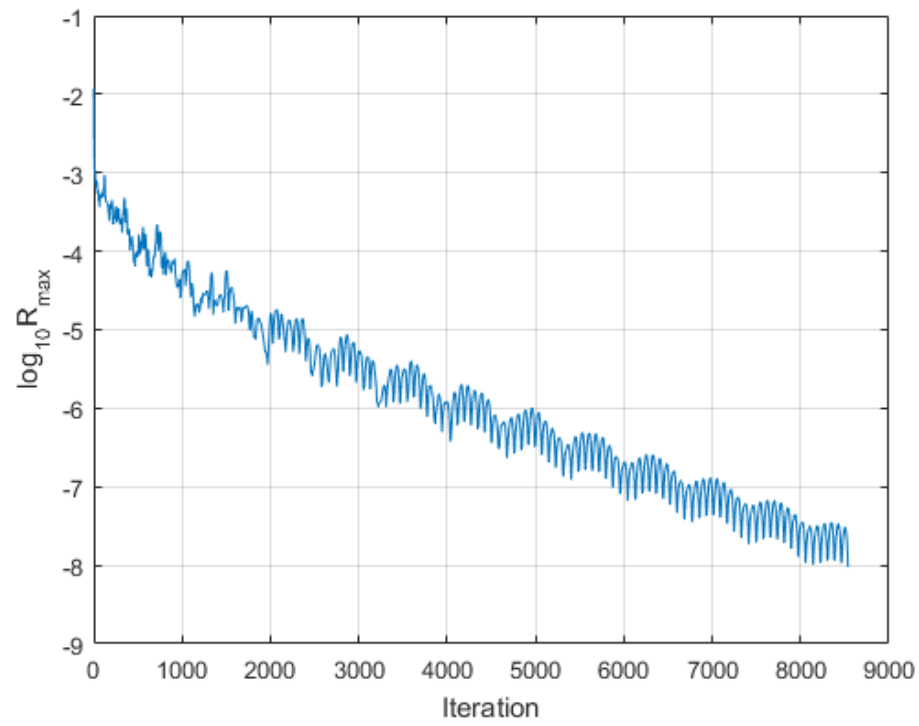
Figure 32: Residual convergence (Second-order finite volume, mesh 0)
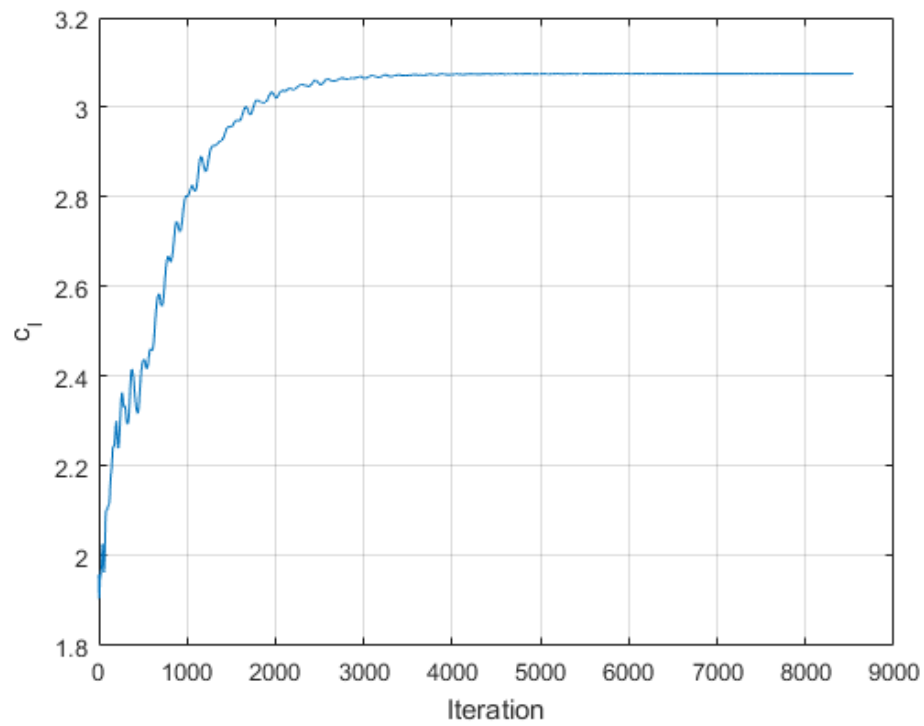
Figure 33: Lift coefficient convergence (Second-order finite volume, mesh 0)

Figure 34: Mach number contours (Second-order finite volume, mesh 0)

Figure 35: Pressure contours (Second-order finite volume, mesh 0)

Figure 36: Surface pressure coefficient distribution (Second-order finite volume, mesh 0)
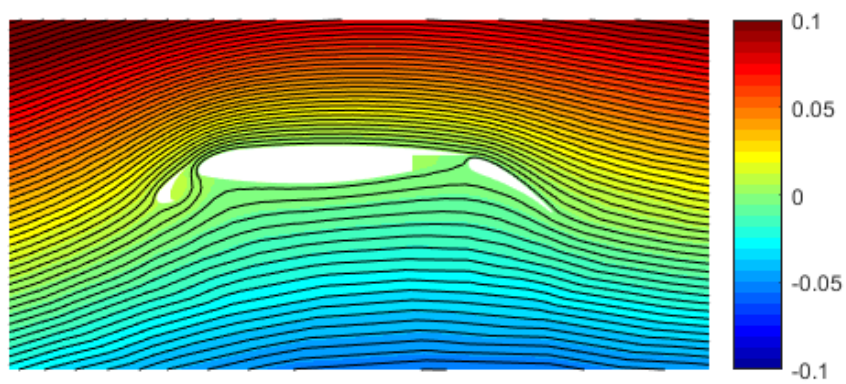

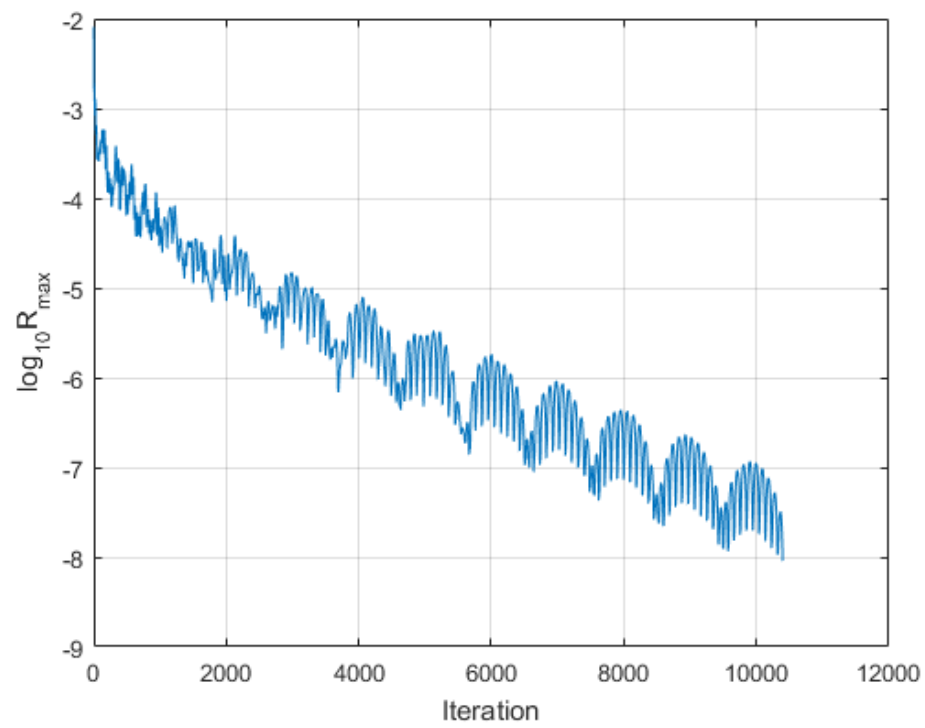Figure 37: Streamline (Second-order finite volume, mesh 0, 50 contours)

Figure 38: Residual convergence (Second-order finite volume, mesh 1)
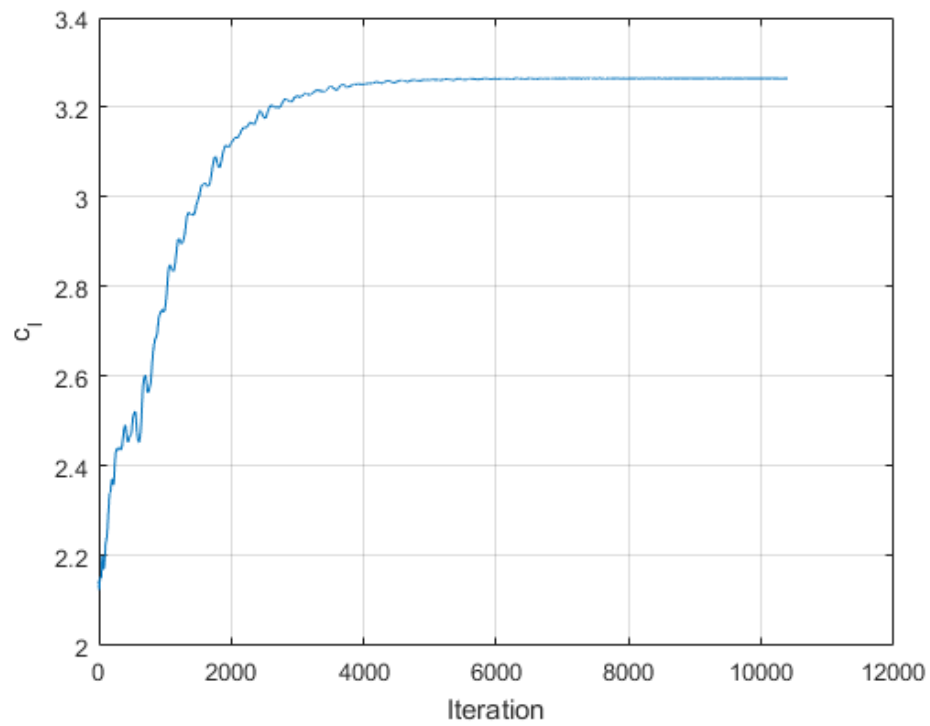

Figure 39: Lift coefficient convergence (Second-order finite volume, mesh 1)
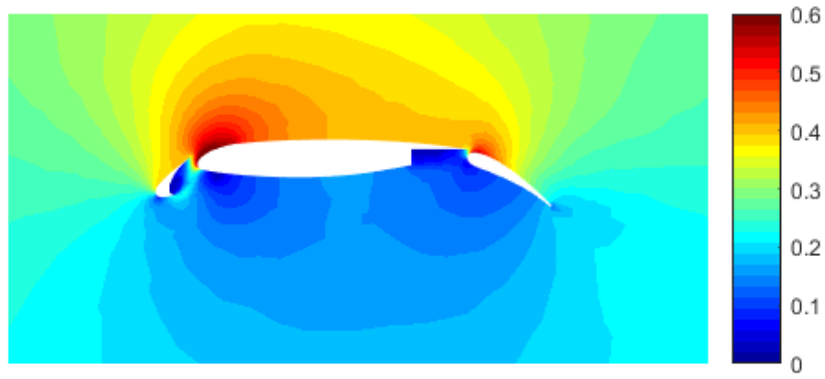
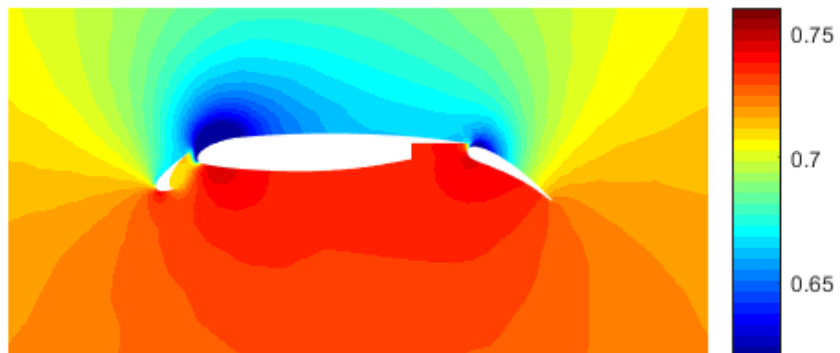Figure 40: Mach number contours (Second-order finite volume, mesh 1)

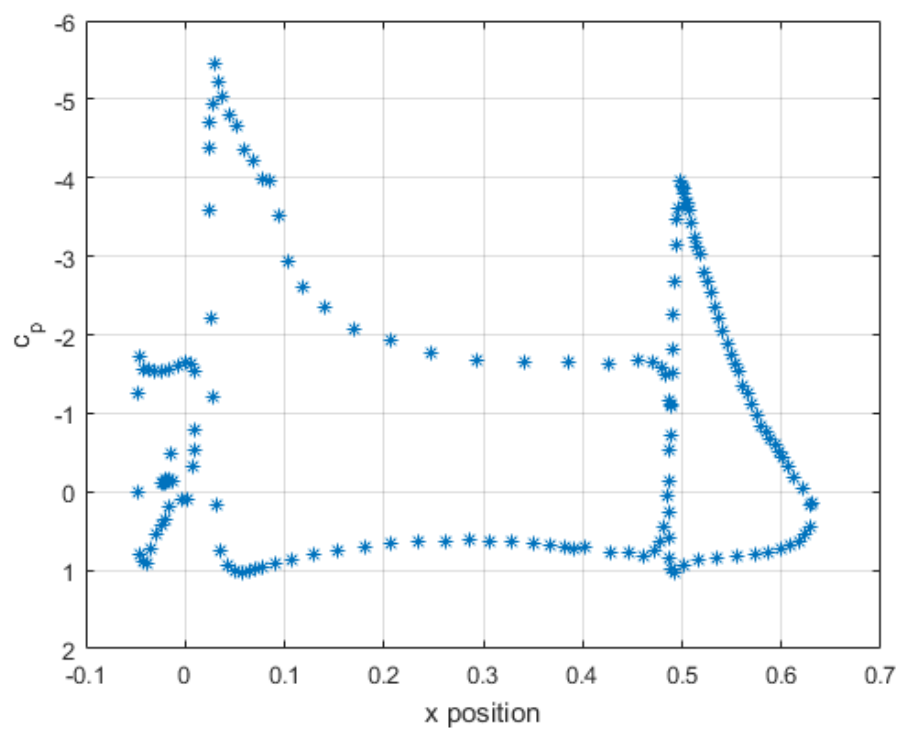Figure 41: Pressure contours (Second-order finite volume, mesh 1)

Figure 42: Surface pressure coefficient distribution (Second-order finite volume, mesh 1)
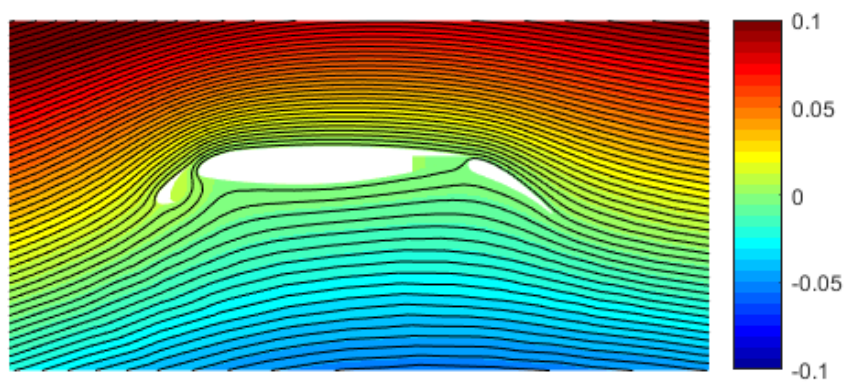

Figure 43: Streamline (Second-order finite volume, mesh 1, 50 contours)

Figure 44: Residual convergence (Second-order finite volume, mesh 2)

Figure 45: Lift coefficient convergence (Second-order finite volume, mesh 2)

Figure 46: Mach number contours (Second-order finite volume, mesh 2)

Figure 47: Pressure contours (Second-order finite volume, mesh 2)

Figure 48: Surface pressure coefficient distribution (Second-order finite volume, mesh 2)

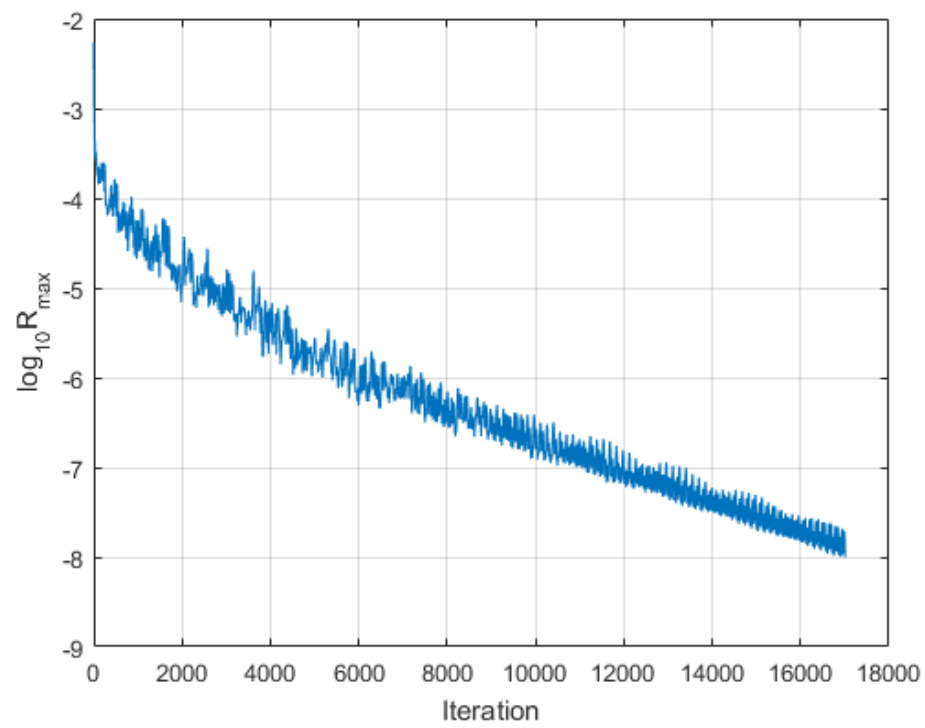Figure 49: Streamline (Second-order finite volume, mesh 2, 50 contours)

Figure 50: Residual convergence (Second-order finite volume, mesh 3)
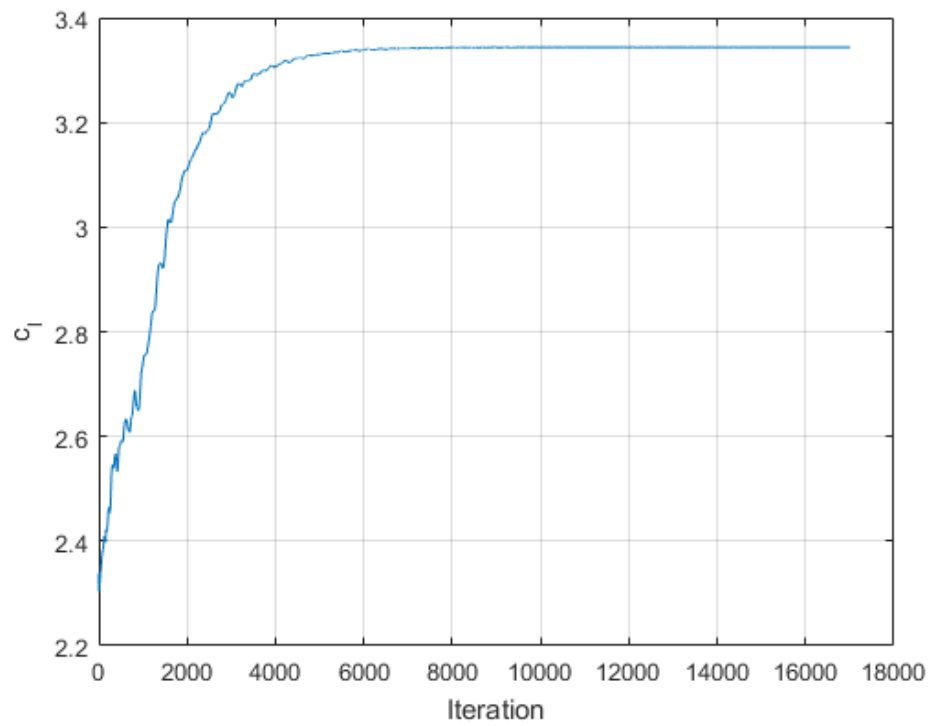

Figure 51: Lift coefficient convergence (Second-order finite volume, mesh 3)
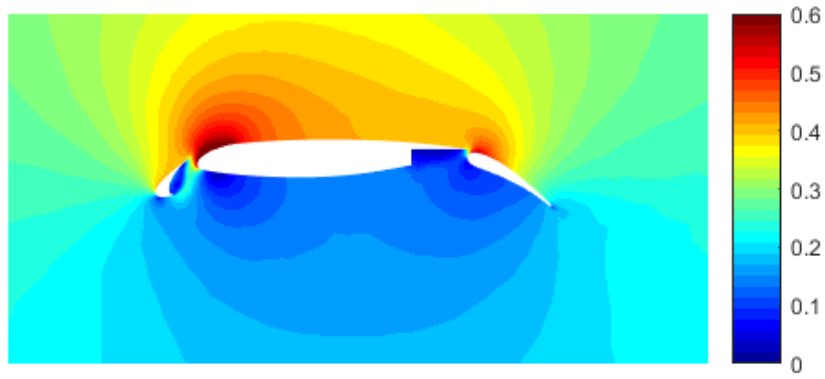
Figure 52: Mach number contours (Second-order finite volume, mesh 3)
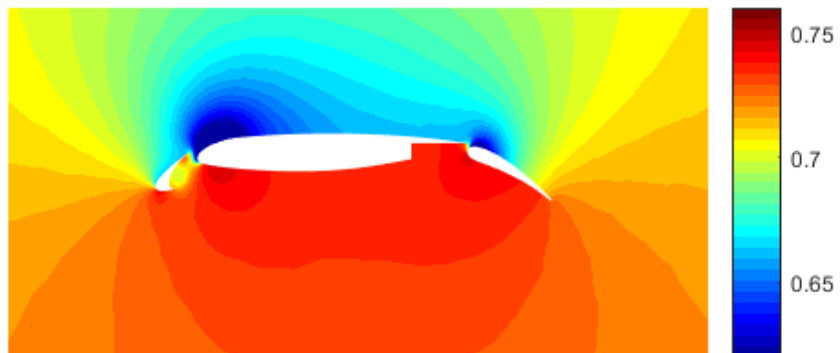

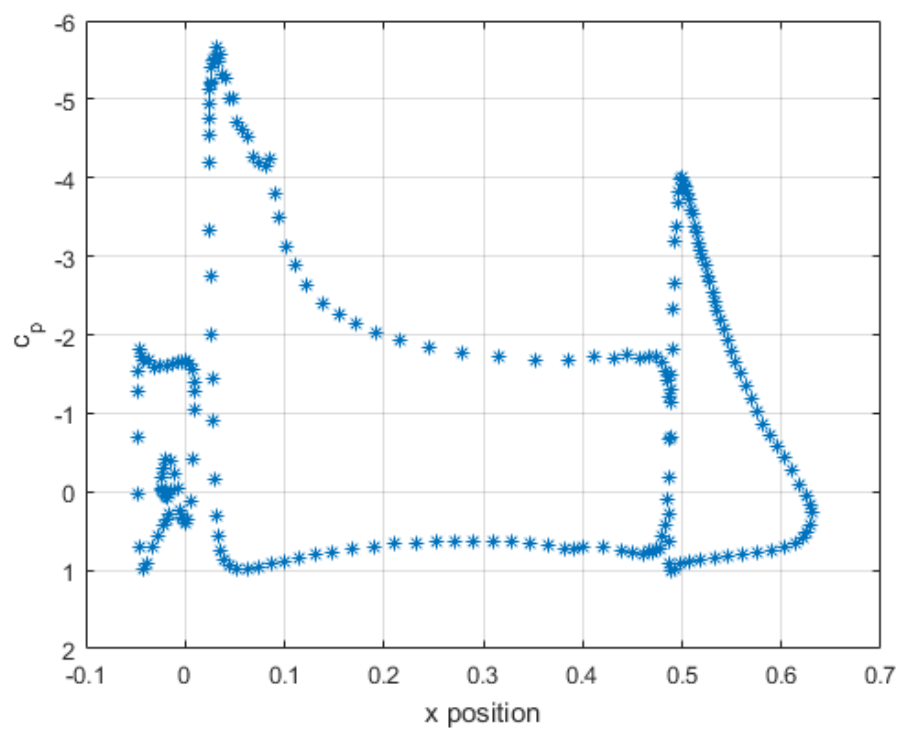Figure 53: Pressure contours (Second-order finite volume, mesh 3)

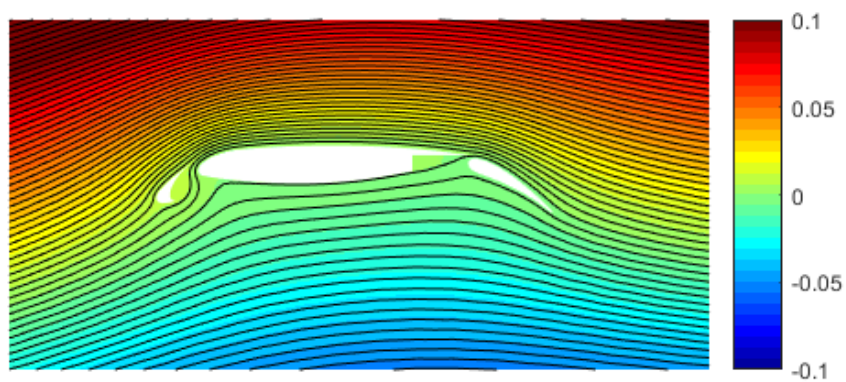Figure 54: Surface pressure coefficient distribution (Second-order finite volume, mesh 3)

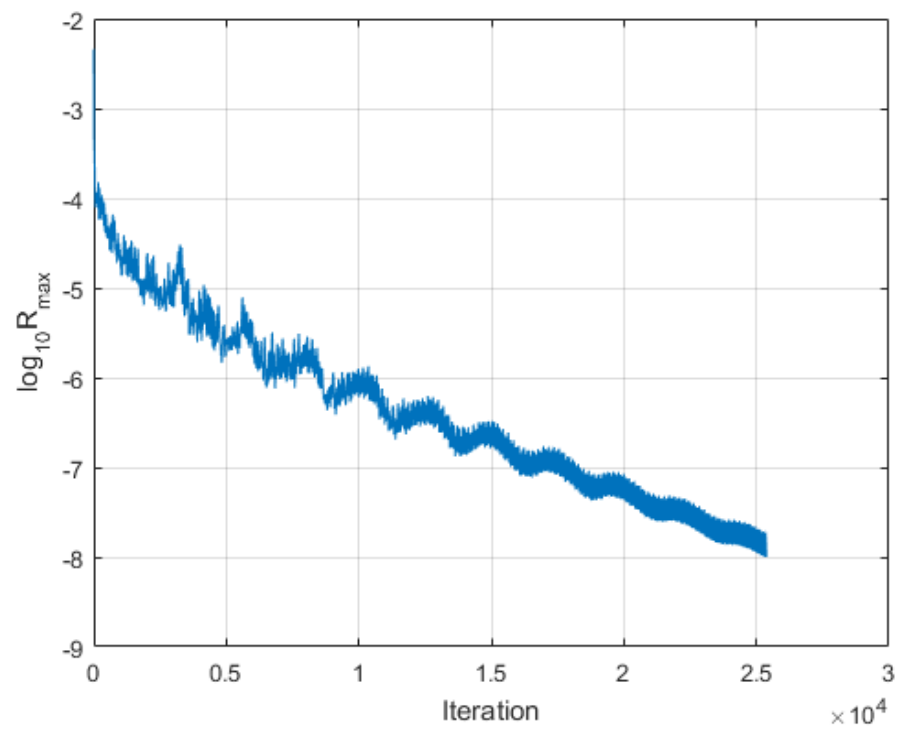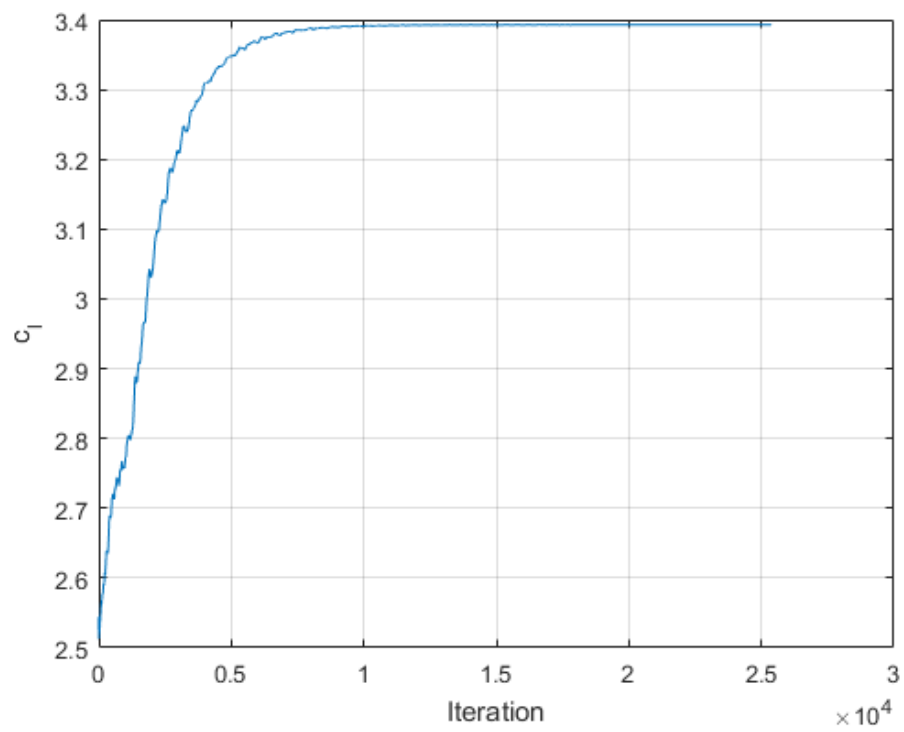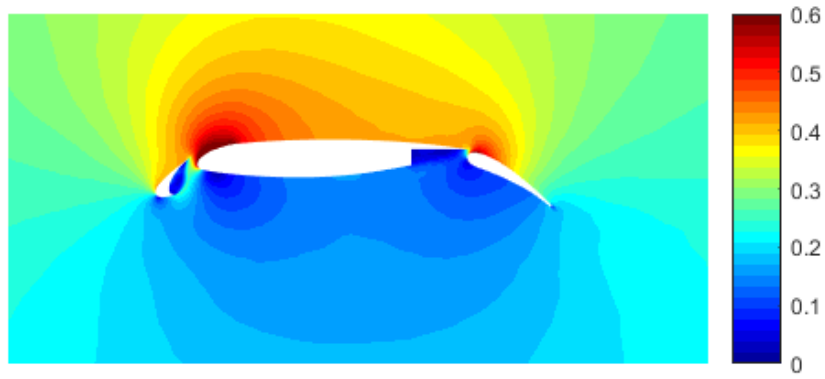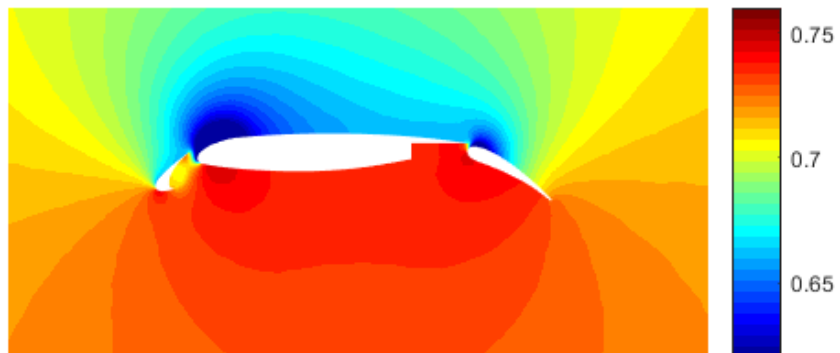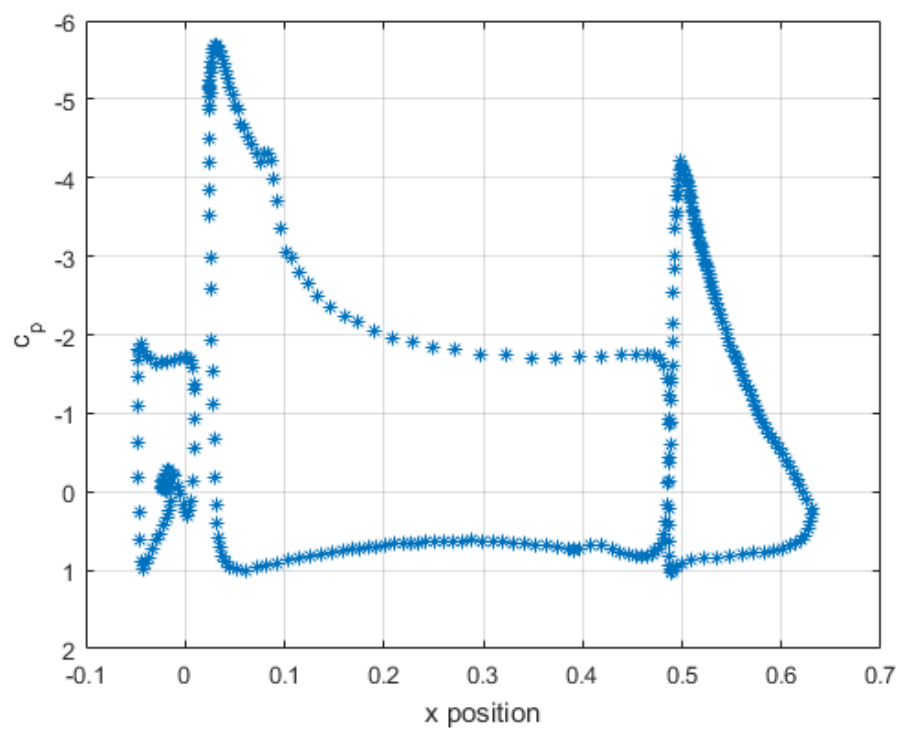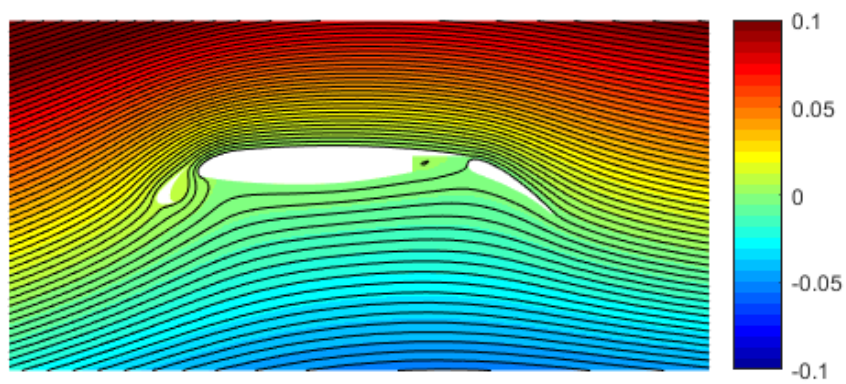Figure 55: Streamline (Second-order finite volume, mesh 3, 50 contours)

Summary of Results

Mesh	First-order Finite-volume			Second-order Finite-volume		
	$c_{l,slat}$	$c_{l,main}$	$c_{l,flap}$	$c_{l,slat}$	$c_{l,main}$	$c_{l,flap}$
0	5.1158e-4	1.5604	0.4025	0.1801	2.3691	0.5258
1	0.0230	1.7072	0.4264	0.2060	2.4747	0.5843
2	0.0549	1.8526	0.4363	0.2103	2.5383	0.5950
3	0.0832	1.9963	0.4659	0.2186	2.5660	0.6081

Table 1: Component lift coefficients

Mesh	First-order Finite-volume			Second-order Finite-volume		
	$c_{d,slat}$	$c_{d,main}$	$c_{d,flap}$	$c_{d,slat}$	$c_{d,main}$	$c_{d,flap}$
0	0.0485	-0.0075	0.2741	-0.1031	-0.1279	0.3060
1	0.0343	-0.0301	0.2772	-0.1296	-0.1489	0.3298
2	0.0173	-0.0649	0.2741	-0.1365	-0.1655	0.3346
3	-0.0055	-0.0902	0.2843	-0.1699	-0.1699	0.3407

Table 2: Component drag coefficients

Mesh	First-order Finite-volume		Second-order Finite-volume	
	$c_{l,total}$	$c_{d,total}$	$c_{l,total}$	$c_{d,total}$
0	1.9634	0.3150	3.0750	0.0751
1	2.1566	0.2814	3.2650	0.0513
2	2.3438	0.2264	3.3437	0.0325
3	2.5453	0.1887	3.3926	0.0235

Table 3: Total lift and drag coefficients

Mesh	First-order Finite-volume		Second-order Finite-volume	
	$\dot{m}_{slat-main}$	$\dot{m}_{main-flap}$	$\dot{m}_{slat-main}$	$\dot{m}_{main-flap}$
0	0.0034	0.0017	0.0064	0.0023
1	0.0041	0.0019	0.0066	0.0025
2	0.0049	0.0020	0.0069	0.0025
3	0.0054	0.0020	0.0069	0.0025

Table 4: Mass flow rates between slat/main and main/flap

Mesh	First-order Finite-volume	Second-order Finite-volume
0	27.5572s	570.5905s
1	77.5342s	1288.0014s
2	254.4730s	3982.2579s
3	759.6846s	11770.4241s

Table 5: Convergence times

The converged solutions showed reasonable lift coefficients, drag coefficients and mass flow rates. As mesh sizes were increased, lift coefficients tend to increase while drag coefficients tend to decrease for slat and main and increase for flap. For both methods, total lift coefficients increased with mesh size and total drag coefficients decreased with mesh size. The mass flow rate, which represents the flow rate of air from below the airfoil to the topside because of a favorable pressure gradient from bottom to top, remains relatively consistent for different mesh sizes in both methods. In convergence times, the results are consistent with what one would expect, that is, increased convergence times for increased mesh sizes.

Conclusion

First and second-order finite volume methods, based on Forward Euler and TVD Second-order Runge-Kutta schemes, were successfully implemented to solve for the conservative states govern by Euler equations. The results show high Mach number flows near the leading edges of the airfoil. A region of high pressure air under the airfoil and a region of low pressure air above the airfoil was also shown in all eight cases, reflecting the high-lift nature of such a wing configuration. Lift and drag coefficients were computed and their respective convergence trends with regard to increasing mesh size were consistent. Mass flow rate between the three components of the airfoil converged to the same number as mesh size was increased. Finally, increased mesh size and increased order translated to longer convergence time for the simulations. For the given meshes, it is expected that the larger the mesh, the better and more accurate the results are, as more mesh is dedicated to areas of interest.